AJS American Journal of Science
publishing earth-sciences research since 1818

Su, B.-X., Xiao, Y., Wang, J., Pan, Q.-Q., & Zhao, S.-Q. (2026). Reversed inter-mineral Fe-Zn isotope fractionation in ophiolitic peridotites: Evidence for widespread hydration of oceanic lithospheric mantle. *American Journal of Science*, *326*, Article 7.
https://doi.org/10.2475/001c.160209

Science Paper

Reversed Inter-Mineral Fe-Zn Isotope Fractionation in Ophiolitic Peridotites: Evidence for Widespread Hydration of Oceanic Lithospheric Mantle

Ben-Xun Su[1,2][a], Yan Xiao[1], Jing Wang[1], Qi-Qi Pan[1], Shou-Qian Zhao[1]

[1] State Key Laboratory of Lithospheric and Environmental Coevolution, Institute of Geology and Geophysics, Chinese Academy of Sciences,
[2] University of Chinese Academy of Sciences

Keywords: Hydration, Fe-Zn isotopes, Ophiolite, Oceanic lithospheric mantle, Elemental exchange

https://doi.org/10.2475/001c.160209

American Journal of Science

Vol. 326, 2026

The oceanic lithospheric mantle is rarely preserved in a pristine, anhydrous state, yet the scale and impact of hydration remain poorly understood. In this study, we identify systematic Fe-Zn isotope anomalies in mantle peridotites and chromitites from the Purang ophiolite (Tibet, China), where silicates (olivine δ^{56}Fe = −0.08 to 0.15‰, δ^{66}Zn = 0.02 to 0.37‰; orthopyroxene δ^{56}Fe = −0.15 to 0.01‰, δ^{66}Zn = 0.05 to 0.26‰; clinopyroxene δ^{56}Fe = 0.04 to 0.17‰, δ^{66}Zn = 0.09 to 0.42‰) exhibit heavier isotope compositions than coexisting spinel (δ^{56}Fe = −0.18 to 0.07‰, , δ^{66}Zn = −0.27 to 0.00‰), a reversal of theoretical predictions and patterns observed in continental mantle peridotite xenoliths. While partial melting and melt metasomatism account for some inter-sample variations, the pervasive inter-mineral fractionation requires hydrous fluid-mediated element exchange, in addition to solidus diffusion, between spinel and silicates. This reversed Fe-Zn isotope fractionation (mirrored in Mg and Cr isotopes) is a widespread feature of ophiolites and abyssal peridotites, reflecting a key characteristic of the oceanic lithospheric mantle. Elevated water contents in ophiolitic olivine, positively correlating with forsterite numbers, further indicate pervasive hydration and associated element exchange. These findings reveal that extensive hydration significantly overprints primary geochemical signatures of melting and melt-rock interaction in the oceanic lithospheric mantle, with its scale and physiochemical impacts historically underestimated.

1. INTRODUCTION

The lithospheric mantle is rarely preserved in a pristine, anhydrous state due to pervasive hydration processes. Recent studies have increasingly recognized hydration as a key mechanism altering mantle rocks, primarily through melt or fluid metasomatism, which introduces water and drives significant modifications in metal isotope compositions (e.g., Cui et al., 2025; Demouchy et al., 2015; J. Liu et al., 2017; Nishi, 2015; Schmädicke et al., 2018; B.-X. Su et al., 2018, 2021, 2025). However, stable metal isotope distributions, particularly Fe and Zn, exhibit striking differences. In continental mantle peridotite xenoliths, Fe isotopes follow a systematic equilibrium fractionation sequence (δ^{56}Fe: spinel > clinopyroxene > orthopyroxene > olivine), consistent with bonding strength controls (Beard & Johnson, 2004; Huang et al., 2011; Macris et al., 2015; Roskosz et al., 2015; Schauble et al., 2001; Williams et al., 2005; Zhao et al., 2012, 2015, 2017). In contrast, ophiolitic mantle peridotites display a reversed Fe isotope sequence, with silicates enriched in heavier isotopes relative to coexisting spinel (Chen et al., 2015; B.-X. Su et al., 2021; Xiao et al., 2016; Zhang et al., 2017). This anomaly extends to Zn and Cr isotopes, which similarly deviate from theoretical predictions (Chen et al., 2019; Fang et al., 2022; Shen et al., 2018; Z.-Z. Wang et al., 2017; Yang et al., 2021).

These reversed isotope fractionations, consistently observed across ophiolites, challenge conventional models of mantle processes and suggest a distinctive characteristic of the oceanic lithospheric mantle. Hydrous fluid-mediated element exchange, potentially linked to chromitite formation or subduction-related fluids, has been proposed as a key driver (Gose & Schmädicke, 2021; B. X. Su et al., 2021; B.-X. Su et al., 2020, 2021, 2023, 2026; in press; Xiao et al., 2023). Yet, the absence of significant chromite deposits in mid-ocean ridges and some ophiolites, coupled with variable fluid sources, indicates that hydration is a complex, multi-faceted process (Cui et al., 2025; B.-X. Su et al., 2023, 2025, 2026). The scale and impact of hydration have historically been underestimated, obscuring its role in reshaping mantle geochemistry. The mechanisms governing inter-mineral isotope fractionation and their connection to

a Corresponding author: subenxun@mail.igcas.ac.cn

pervasive hydration remain unsolved, limiting our understanding of oceanic lithospheric mantle evolution.

This study presents high-precision Fe and Zn isotope data from coexisting minerals (spinel, orthopyroxene, clinopyroxene, and olivine) in mantle rocks from an ophiolite in Tibetan Plateau. By integrating these data with global ophiolite records, we elucidate the controls on inter-mineral isotope fractionation, revealing hydrous fluid-mediated element exchange as a widespread process in the oceanic lithospheric mantle. Our findings highlight the transformative role of hydration, demonstrating its profound impact on mantle geochemistry and necessitating a revised framework for interpreting oceanic mantle processes.

2. PURANG OPHIOLITE AND SAMPLES

The Purang ophiolite is located in the Yarlung-Zangbo Suture zone in the Tibetan Plateau (fig. 1A, B). It exposes a well-preserved mantle sequence dominated by harzburgites with subordinate lherzolites and dunites (fig. 1C; C.-Z. Liu et al., 2010; F. Liu et al., 2015). Our samples, largely unaltered (figs. 2, S1) have been previously characterized for petrography and elemental geochemistry (B. X. Su et al., 2019; B.-X. Su et al., 2015) and are briefly summarized here. The lherzolites and harzburgites have similar mineral assemblages with differences in modal contents of clinopyroxene, and their orthopyroxene grains are highly variable in size from <1 mm to >2.5 cm (fig. 2A–D). The dunites and chromitites are commonly associated with each other and consist exclusively of olivine and spinel, with minor amounts of serpentine in a few samples (fig. 2E–H). Spinel, orthopyroxene, clinopyroxene, and olivine were separated from 4 lherzolites, 7 harzburgites, 6 dunites, and 5 chromitites from the Purang ophiolite for Fe and Zn isotope analyses. The major oxide mineral chemistry of the Purang lherzolites and harzburgites is very similar (B. X. Su et al., 2019; B.-X. Su et al., 2015). Olivine in the lherzolites and harzburgites has forsterite (Fo) contents of 90.5–92 and shows no apparent correlation with NiO contents, whereas olivine in the dunites and chromitites has a slightly larger variation in Fo (90–93) and exhibits a positive correlation between Fo and NiO. All spinel grains in the studied samples are high-Al varieties with Cr# (100×Cr/(Cr+Al)) values of 15.8 to 50.1. Orthopyroxenes generally have variable CaO and Al_2O_3 contents and Cr#s and show weak or no correlation with Mg# values (100×Mg/(Mg+Fe); 89.7 to 91.8). Clinopyroxene compositions in the Purang samples are highly variable, such as Mg# = 91.1 to 94.4 (B. X. Su et al., 2019).

3. ANALYTICAL METHODS

Fe-Zn isotopic analyses were conducted at Metallogenic Elements and Isotopes Laboratory in the Institute of Geology and Geophysics, Chinese Academy of Sciences, following the protocol described in J. Wang et al. (2022, 2023). 6–200 mg of minerals were weighed. The spinel was preprocessed using a M6 Microwave Oven (PreeKem, China) with mixture of concentrated 4.5 mL HCl, 1.5 mL HNO_3, 3 mL HF and 1 mL $HClO_4$. And then followed the general routine like other minerals concentrated HNO_3 and HF acids in 7 mL PTFE Teflon square digestion vessels at 160 °C for 2 days. Following the evaporation of HNO_3 and HF, the samples were subsequently treated with HNO_3 and HCl (1:3) and refluxed at 80 °C for 1 day. Then the samples were dried down and redissolved in 1 mL concentrated HCl at 130 °C. Finally, the samples were dried down again and brought into solution in 8 M HCl (+0.001% H_2O_2) for chemical purification. Fe and Zn were purified using a two-step ion exchange chromatography. The solution was loaded onto pre-conditioned 2 mL Bio-Rad AG-MP-1M resin first. Matrix elements were eluted in the next 9 mL of 8 M HCl. Fe fraction was collected in 18 mL of 2 M HCl. After that, 2 mL of 0.5 M HNO_3 was added to resin and Zn fraction was collected in 10 mL of 0.5 M HNO_3 sequentially. Fe and Zn fractions were evaporated to dryness and then redissolved in 1 mL of 8 M HCl (+0.001% H_2O_2) separately for second chemical purification. They were loaded onto pre-conditioned 1 mL Bio-Rad AG-1-X8 resin for second purification. 9 mL of 8 M HCl was used to elute the matrix elements and Fe fraction was collected in the next 10 mL of 0.4 M HCl. Zn fraction was collected in 7 mL of 0.5 M HNO_3 afterwards. The final Fe and Zn eluates were evaporated to dryness and diluted in 2% HNO_3 to 30 ng g^{-1} (Fe) or 500 ng g^{-1} (Zn) for isotopic measurements. The total procedure blank for Fe and Zn isotope analyses are 5 ng and 6 ng, respectively.

Fe and Zn isotopic measurements were performed on Nu Sapphire CC-MC-ICP-MS at the conventional pathway (Zn) or the collision cell pathway (Fe) in low resolution mode using the sample-standard bracketing method. Data were collected in static mode, with connected to pre-amplifiers fitted with 10^{11} Ω resistor. Each analysis consisted of a block with 50 cycles of 3 s integration. A 30 s (Zn) or 50 s (Fe) wash was performed in 2% HNO_3 between each standard and sample to avoid cross contamination. Long-term reproducibility is 0.03‰ (2sd) for Fe and Zn isotopic measurements. The Fe and Zn isotope results were reported as the per mil deviation relative to standard IRMM-014 and JMC 3-0749L, respectively. The results of samples are presented in table 1, and geostandards in table 2. The values of geostandards are consistent with previous results (J. Wang et al., 2022, 2023 and references therein).

4. RESULTS

The Fe isotope compositions of the Purang ophiolite suite reveal mineral-scale fractionations across lherzolites, harzburgites, dunites and chromitites (fig. 3; table 1). In lherzolites, olivine is enriched in heavy Fe isotopes, with δ^{56}Fe values ranging from 0.05‰ to 0.08‰, while coexisting spinel is isotopically lighter, with δ^{56}Fe values between −0.10‰ and −0.06‰. Orthopyroxene exhibits intermediate δ^{56}Fe values from −0.15‰ to 0.00‰, and clinopyroxene shows much higher δ^{56}Fe values of 0.04‰ to 0.17‰. Harzburgites display a similar pattern: olivine δ^{56}Fe ranges from 0.02‰ to 0.14‰, spinel from −0.18‰ to −0.04‰, orthopyroxene from −0.13‰ to 0.01‰, and clinopyroxene from 0.06‰ to 0.15‰. In dunites, olivine δ^{56}Fe spans

Table 1. Fe and Zn isotope compositions of olivine (Ol), orthopyroxene (Opx), spinel (Sp), and clinopyroxene (Cpx) in lherzolites, harzburgites, dunites, and chromitites from Purang ophiolite

Sample	Rock type	Mineral	δ^{56}Fe	2sd	N	δ^{66}Zn	2sd	δ^{68}Zn	2sd	N	Sample	Rock type	Mineral	δ^{56}Fe	2sd	N	δ^{66}Zn	2sd	δ^{68}Zn	2sd	N
PL14-5-1	Lherzolite	Ol	0.08	0.03	4	0.23	0.03	0.43	0.04	4	PL14-5-1	Lherzolite	Sp	-0.08	0.03	4	-0.20	0.05	-0.42	0.01	3
PL14-5-2	Lherzolite	Ol	0.07	0.04	4	0.20	0.06	0.45	0.00	3	PL14-5-2	Lherzolite	Sp	-0.09	0.02	4	-0.25	0.03	-0.48	0.05	4
PL14-5-7	Lherzolite	Ol	0.06	0.03	4	0.31	0.03	0.62	0.04	4	PL14-5-7	Lherzolite	Sp	-0.06	0.03	4	-0.22	0.03	-0.44	0.04	3
PL14-5-4	Lherzolite	Ol	0.05	0.03	4	0.23	0.03	0.42	0.02	4	PL14-5-4	Lherzolite	Sp	-0.10	0.01	4	-0.20	0.05	-0.43	0.07	4
PL14-5-11	Harzburgite	Ol	0.02	0.02	4	0.12	0.05	0.26	0.00	4	PL14-5-11	Harzburgite	Sp	-0.04	0.03	3	-0.11	0.05	-0.20	0.04	3
PL14-5-3	Harzburgite	Ol	0.03	0.01	3	0.22	0.04	0.47	0.05	4	PL14-5-3	Harzburgite	Sp	-0.12	0.01	4	-0.18	0.03	-0.38	0.05	4
PL14-1-3	Harzburgite	Ol	0.04	0.02	3	0.37	0.06	0.75	0.04	3	PL14-1-3	Harzburgite	Sp	-0.16	0.02	4	-0.24	0.03	-0.52	0.07	3
PL14-1-3-R	Harzburgite	Ol	0.05	0.02	4	0.35	0.03	0.69	0.02	3	PL14-1-3-r	Harzburgite	Sp	-0.18	0.03	4	-0.23	0.03	-0.47	0.03	3
PL14-5-6	Harzburgite	Ol	0.04	0.03	4	0.17	0.04	0.36	0.04	4	PL14-5-6	Harzburgite	Sp	-0.05	0.04	4	-0.15	0.04	-0.33	0.04	3
PL14-5-6-r	Harzburgite	Ol	-0.01	0.01	4						PL14-5-16	Harzburgite	Sp	-0.06	0.02	4	-0.13	0.03	-0.27	0.07	3
PL14-5-16	Harzburgite	Ol	0.06	0.03	4	0.30	0.01	0.59	0.07	3	PL14-2-1	Harzburgite	Sp	-0.08	0.04	4	-0.27	0.04	-0.55	0.06	3
PL14-5-16-R	Harzburgite	Ol	0.05	0.03	4	0.27	0.04	0.55	0.07	3	PL14-2-1-r	Harzburgite	Sp	-0.08	0.03	4					
PL14-2-1	Harzburgite	Ol	0.07	0.04	4	0.11	0.03	0.21	0.05	3	PL14-2-1-R	Harzburgite	Sp	-0.09	0.02	4	-0.23	0.04	-0.46	0.04	3
PL14-2-1-r	Harzburgite	Ol				0.12	0.04	0.24	0.06	4	PL14-5-9	Harzburgite	Sp	-0.05	0.02	4	-0.06	0.05	-0.12	0.01	3
PL14-5-9	Harzburgite	Ol	0.14	0.01	4	0.19	0.05	0.38	0.06	3	PL14-3-1	Dunite	Sp	0.04	0.02	4	0.09	0.05	0.16	0.02	3
PL14-3-1	Dunite	Ol	0.12	0.03	4	0.27	0.04	0.53	0.08	4	PL14-3-1-R	Dunite	Sp				0.07	0.02	0.15	0.04	3
PL14-5-17	Dunite	Ol	-0.06	0.03	3	0.13	0.04	0.25	0.03	3	PL14-5-17	Dunite	Sp	-0.12	0.02	4	-0.10	0.03	-0.20	0.03	3
PL14-5-19	Dunite	Ol	-0.07	0.04	4	0.29	0.03	0.59	0.04	4	PL14-5-19	Dunite	Sp	0.01	0.01	4	-0.06	0.03	-0.11	0.05	3
PL14-5-19-R	Dunite	Ol	-0.07	0.04	4	0.25	0.03	0.51	0.02	4	PL14-3-2	Dunite	Sp	-0.11	0.02	4	-0.21	0.04	-0.44	0.03	3
PL14-3-2	Dunite	Ol	-0.08	0.02	4	0.10	0.04	0.21	0.05	4	PL14-5-10	Dunite	Sp	-0.11	0.02	4	-0.01	0.04	-0.04	0.03	3
PL14-5-10	Dunite	Ol	-0.08	0.04	3	0.02	0.04	0.04	0.04	3	PL14-5-12	Dunite	Sp	-0.03	0.02	4	-0.01	0.05	-0.02	0.06	3
PL14-5-12	Dunite	Ol	-0.08	0.03	4	0.26	0.06	0.60	0.21	2	PL14-5-12-r	Dunite	Sp	0.03	0.03	4					
PL14-5-8	Chromitite	Ol	-0.01	0.03	4	0.27	0.03	0.54	0.05	3	PL14-5-8	Chromitite	Sp	0.05	0.03	4	0.00	0.02	-0.01	0.00	3
PL14-5-18	Chromitite	Ol	0.02	0.01	3	0.27	0.05	0.57	0.08	3	PL14-5-8-R	Chromitite	Sp	0.07	0.04	4	-0.02	0.05	-0.04	0.05	3
PL14-5-20	Chromitite	Ol	0.03	0.04	4	0.13	0.03	0.26	0.00	3	PL14-5-18	Chromitite	Sp	0.00	0.03	4	-0.11	0.03	-0.23	0.03	4
PL14-5-20-R	Chromitite	Ol	-0.03	0.04	4	0.09	0.04	0.22	0.05	3	PL14-5-18-r	Chromitite	Sp				-0.09	0.03	-0.17	0.05	3
PL14-5-15	Chromitite	Ol	0.07	0.02	4	0.31	0.03	0.62	0.05	5	PL14-5-20	Chromitite	Sp	-0.02	0.02	4	0.00	0.03	-0.01	0.06	3
PL14-1-5	Chromitite	Ol	0.15	0.03	4	0.24	0.04	0.50	0.04	3	PL14-5-15	Chromitite	Sp	0.00	0.03	4	0.03	0.04	0.06	0.03	3
PL14-1-5-r	Chromitite	Ol	0.15	0.05	4						PL14-1-5	Chromitite	Sp	0.07	0.03	4	-0.10	0.06	-0.20	0.06	3
PL14-5-1	Lherzolite	Opx	-0.13	0.04	4	0.18	0.05	0.33	0.04	3	PL14-1-5-r	Chromitite	Sp				-0.16	0.02	-0.32	0.01	3
PL14-5-2	Lherzolite	Opx	-0.15	0.03	4	0.21	0.03	0.45	0.02	4	PL14-5-1	Lherzolite	Cpx	0.07	0.01	4	0.10	0.02	0.20	0.02	3
PL14-5-7	Lherzolite	Opx	-0.15	0.02	4	0.16	0.03	0.34	0.05	3	PL14-5-1-r	Lherzolite	Cpx	0.04	0.02	4					
PL14-5-4	Lherzolite	Opx	0.00	0.02	3	0.12	0.03	0.28	0.05	4	PL14-5-2	Lherzolite	Cpx	0.17	0.02	4					
PL14-5-4-r	Lherzolite	Opx	0.00	0.03	4						PL14-5-7	Lherzolite	Cpx	0.05	0.04	3	0.13	0.07	0.27	0.04	3
PL14-5-11	Harzburgite	Opx	-0.13	0.03	4	0.05	0.05	0.12	0.00	3	PL14-5-4	Lherzolite	Cpx	0.12	0.03	4	0.09	0.03	0.20	0.07	3
PL14-5-3	Harzburgite	Opx	-0.03	0.03	3	0.17	0.02	0.38	0.04	3	PL14-5-4-r	Lherzolite					0.13	0.05	0.24	0.05	3
PL14-1-3	Harzburgite	Opx	0.01	0.03	4	0.25	0.02	0.49	0.01	3	PL14-5-3	Harzburgite	Cpx	0.06	0.02	4	0.16	0.03	0.32	0.05	5

Sample	Rock type	Mineral	δ^{56}Fe	2sd	N	δ^{66}Zn	2sd	δ^{68}Zn	2sd	N	Sample	Rock type	Mineral	δ^{56}Fe	2sd	N	δ^{66}Zn	2sd	δ^{68}Zn	2sd	N
PL14-5-6	Harzburgite	Opx	-0.10	0.03	4	0.12	0.02	0.26	0.02	4	PL14-5-3-r	Harzburgite	Cpx	0.09	0.03	3					
PL14-5-16	Harzburgite	Opx	-0.07	0.04	4	0.23	0.05	0.47	0.03	3	PL14-5-6	Harzburgite	Cpx	0.13	0.03	4	0.42	0.01	0.87	0.04	2
PL14-5-16-R	Harzburgite	Opx	-0.02	0.03	4	0.20	0.02	0.41	0.01	3	PL14-5-6-R	Harzburgite	Cpx	0.15	0.02	4	0.39	0.04	0.82	0.04	3
PL14-2-1	Harzburgite	Opx	-0.06	0.03	4	0.15	0.03	0.30	0.03	3	PL14-2-1	Harzburgite	Cpx	0.13	0.02	4	0.10	0.03	0.22	0.05	4
PL14-5-9	Harzburgite	Opx	-0.04	0.03	4	0.26	0.02	0.54	0.05	4	PL14-2-1-r	Harzburgite	Cpx				0.09	0.02	0.21	0.04	2

R-Replicate: repeat sample dissolution, column chemistry and instrumental analyses; r-duplicate: repeat analysis on the same purified sample solution during different analytical sessions.

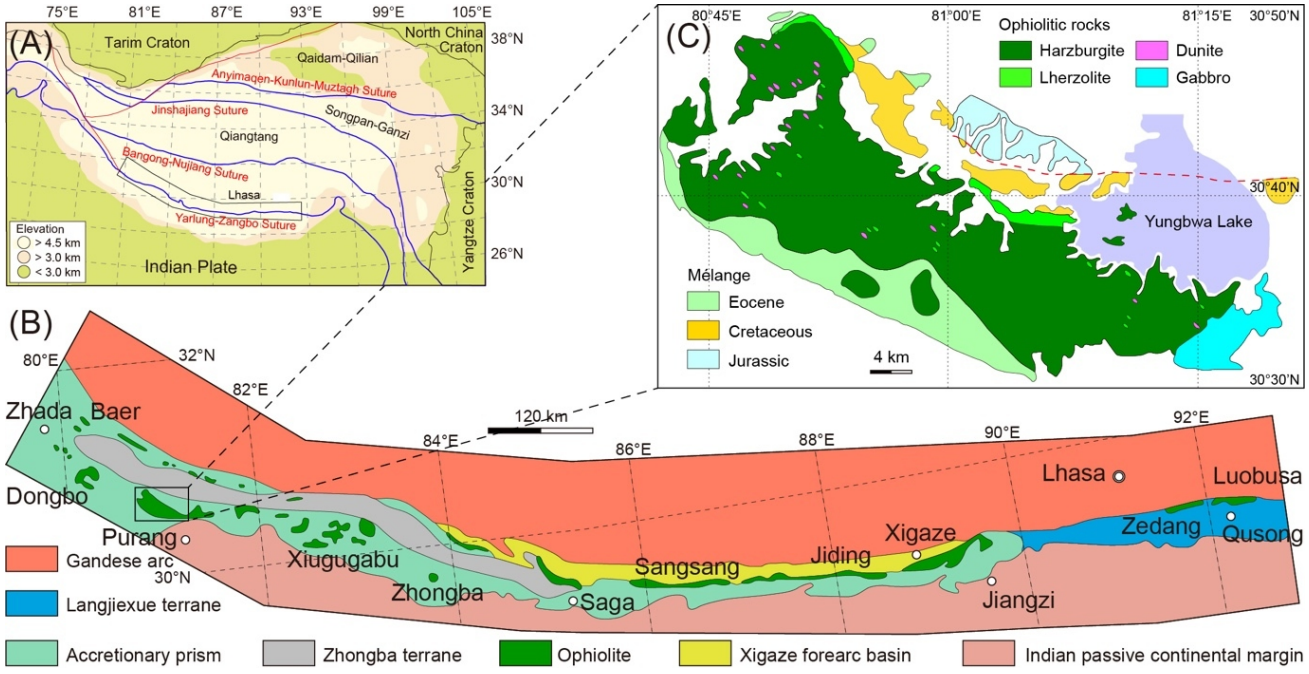

Figure 1. (A) Tectonic sketch map of Tibetan Plateau, highlighting major suture zones. (B) Distribution of ophiolites within the Yarlung-Zangbo Suture Zone, southern Tibet. (C) Geologic map of the Purang ophiolite (modified after Hebei Institute of Geological Survey, 2006), illustrating the spatial arrangement of mantle sequences dominated by harzburgites with subordinate lherzolites and dunites.

−0.08‰ to 0.12‰, and spinel ranges from −0.12‰ to 0.04‰. Chromitites show olivine δ^{56}Fe values from −0.03‰ to 0.15‰ and spinel δ^{56}Fe from −0.02‰ to 0.07‰.

Zn isotope compositions mirror the Fe isotope trends, with a clear light-heavy partitioning (fig. 3; table 1). In lherzolites, olivine δ^{66}Zn spans 0.20‰ to 0.31‰, while spinel is isotopically light, with δ^{66}Zn of −0.25‰ to −0.20‰. Orthopyroxene has moderate δ^{66}Zn values between 0.12‰ and 0.21‰, and clinopyroxene ranges from 0.09 ‰to 0.13‰. In harzburgites, Zn isotopic compositions of minerals vary from 0.11‰ to 0.37‰ for olivine, from −0.27‰ to −0.06‰ for spinel, from 0.05‰ to 0.26‰ for orthopyroxene, and from 0.09‰ to 0.42‰ for clinopyroxene. Dunites exhibit greater scatter in olivine δ^{66}Zn (0.02‰ to 0.29‰), with spinel ranging from −0.21‰ to −0.01‰. In chromitites, olivine δ^{66}Zn spans 0.09‰ to 0.31‰, while spinel δ^{66}Zn ranges from −0.10‰ to 0.00‰.

5. DISCUSSION

5.1. Widespread reversed inter-mineral fractionation of Fe-Zn isotopes in oceanic lithospheric mantle

Global isotope data compilations highlight a consistent pattern of reversed Fe-Zn isotope fractionation in oceanic lithospheric mantle, distinct from continental mantle peridotite xenoliths (fig. 3). In ophiolitic lherzolites, harzburgites, dunites, and chromitites, olivine exhibits δ^{56}Fe values (fig. 3A) typically higher than or within the average upper mantle range (0.02 ± 0.03‰; Weyer & Ionov, 2007), while coexisting spinel displays a broader δ^{56}Fe range, predominately lighter than this benchmark (fig. 3A). The Purang ophiolite reinforces this trend, with olivine isotopically heavier than spinel, and clinopyroxene showing notably elevated δ^{56}Fe values compared to other coexisting minerals (table 1). Orthopyroxene δ^{56}Fe values generally exceed those of spinel, though some outliers with lower δ^{56}Fe are noted and discussed later. This silicate > spinel δ^{56}Fe sequence in ophiolitic rocks inverts the bonding-strength-driven equilibrium fractionation (Macris et al., 2015; Roskosz et al., 2015; Schauble et al., 2001) observed in mantle peridotite xenoliths (fig. 3A).

Zinc isotopes exhibit even sharper contrasts. In mantle peridotite xenoliths, spinel is enriched in heavier Zn isotopes relative to olivine, orthopyroxene and clinopyroxene, all of which align closely with the average upper mantle δ^{66}Zn (0.18 ± 0.08‰; Sun et al., in press) (fig. 3B) and follow bonding-strength predictions (Fang et al., 2022; Z.-Z. Wang et al., 2017; Yang et al., 2021). Conversely, ophiolitic spinel and olivine show δ^{66}Zn values extending to significantly lighter and heavier compositions, respectively, far beyond the average upper mantle range (fig. 3B). While pyroxene δ^{66}Zn values in ophiolitic rocks resemble those in xenoliths (Fang et al., 2022; Z.-Z. Wang et al., 2017), their consistently heavier compositions than coexisting spinel distinguish oceanic from continental mantle mineral pairs (fig. 3B).

This reversed Fe and Zn isotope fractionation is not exclusive to ophiolites but also evident in abyssal and orogenic peridotites, albeit with limited data (Fang et al., 2022; Yang et al., 2021). Abyssal peridotites mirror ophiolitic olivine-spinel Zn isotope patterns, while orogenic peridotites show heavy olivine and comparable pyroxene δ^{66}Zn

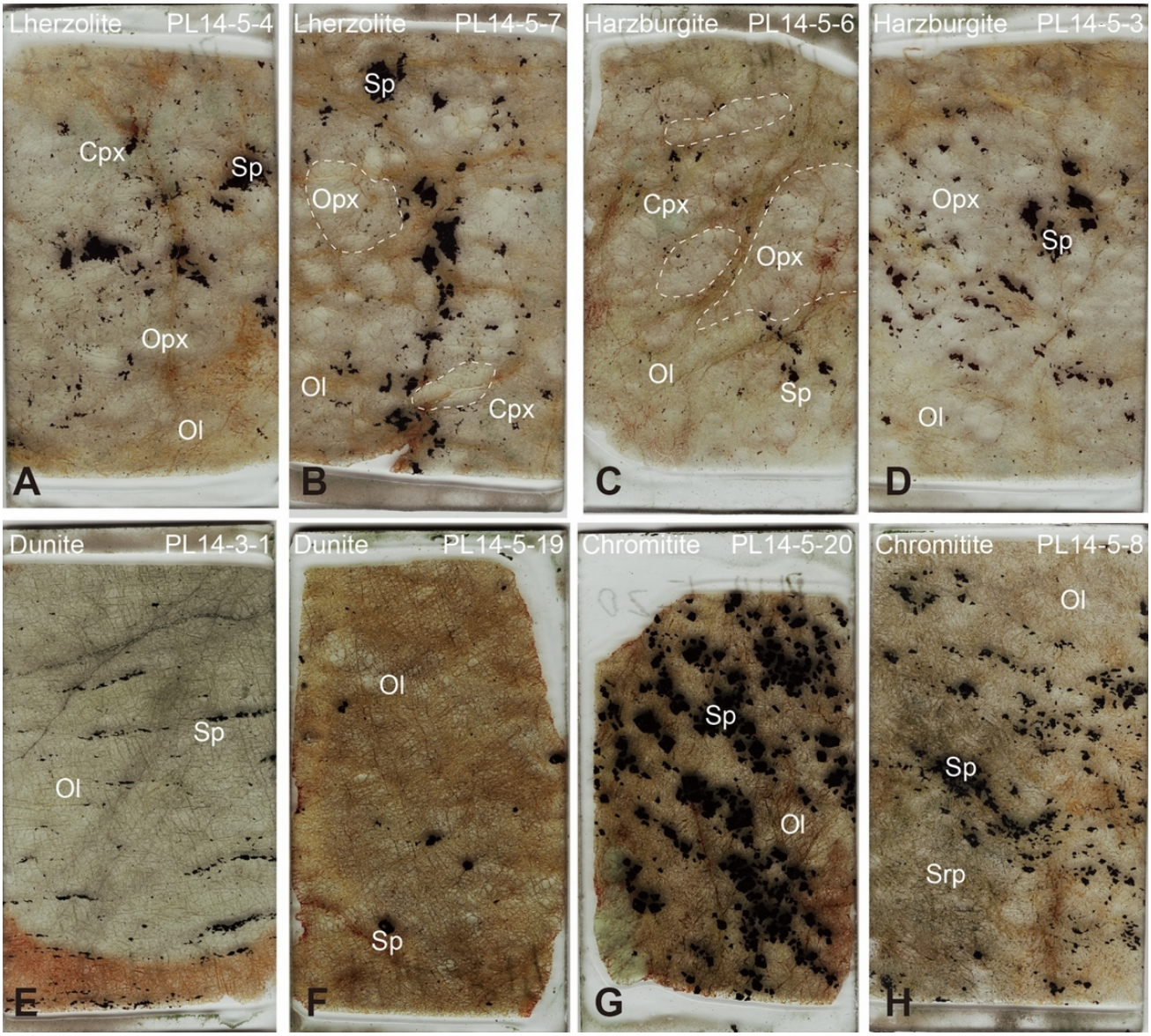

Figure 2. Scanned thin-section images of representative samples from the Purang ophiolite, illustrating mineral assemblages and textural variations (width of thin sections ~2.5 cm.). (A, B) Lherzolites composed of olivine (Ol), orthopyroxene (Opx), clinopyroxene (Cpx), and spinel (Sp), with larger Opx grains (0.5–1 cm) in sample PL14-5-7 compared to PL14-5-4; (C, D) Harzburgites containing Ol, Opx, Sp and minor Cpx, with larger Opx grains (1–2.5 cm) in sample PL14-5-6 relative to PL14-5-3; (E, F) Dunites consisting of Ol and Sp, with serpentinization evident in sample PL14-5-19; (G, H) Chromitites primarily composed of Sp and Ol, with increased serpentine (Srp) content in sample PL14-5-8.

relative to ophiolitic counterparts (fig. 3B). Given that ophiolitic, abyssal, and orogenic peridotites are all representative of oceanic lithospheric mantle, this reversed inter-mineral fractionation appears widespread, pointing to a process distinct from equilibrium fractionation or simple melt/fluid-rock interaction. Notably, the magnitude of inter-mineral isotope fractionation in oceanic lithospheric mantle surpasses that in continental settings (fig. 3), implying a potentially fundamental geochemical distinction between them.

5.2. Effects of grain size and serpentinization on mineral Fe-Zn isotopes

In the Purang ophiolite, most samples exhibit reversed Fe-Zn isotope fractionation between silicate and spinel, but certain lherzolites and harzburgites (e.g., samples PL14-5-7 and PL14-5-6) display orthopyroxene with lower δ^{56}Fe than coexisting spinel (fig. 4A). Petrographic analysis reveals that these samples contain unusually large orthopyroxene grains (0.5–2.5 cm) compared to others (< 0.5 cm) (figs. 2B, C, S1). The large grain size likely limited isotope modification, preserving a δ^{56}Fe closer to primary compositions. In contrast, Zn isotope compositions of these orthopyroxene grains align with those of smaller grains (fig. 3B), likely

Table 2. Fe and Zn isotope compositions of standard references

Sample	δ^{56}Fe	2sd	N	δ^{66}Zn	2sd	δ^{68}Zn	2sd	N
BIR-1	0.06	0.02	4	0.16	0.04	0.34	0.07	3
BCR-2	0.08	0.04	4	0.25	0.01	0.48	0.06	3
W-2	0.01	0.03	4	0.19	0.04	0.41	0.04	3
BHVO-2	0.08	0.02	4	0.27	0.01	0.58	0.00	3
BIR-1	0.06	0.01	4	0.25	0.03	0.48	0.07	3
BIR-1	0.04	0.04	4	0.24	0.00	0.47	0.03	3
NOD-P-1	-0.60	0.02	4	0.74	0.02	1.45	0.07	3
W-2	0.05	0.03	3	0.17	0.04	0.34	0.04	3
NOD-A-1	-0.40	0.02	4	0.88	0.05	1.96	0.06	3
NOD-P-1	-0.57	0.03	4	0.68	0.05	1.39	0.08	3
BCR-2	0.05	0.01	4	0.22	0.02	0.46	0.02	3
W-2	0.04	0.01	4	0.19	0.05	0.35	0.07	4
NOD-A-1	-0.39	0.02	4	0.90	0.03	1.76	0.07	3

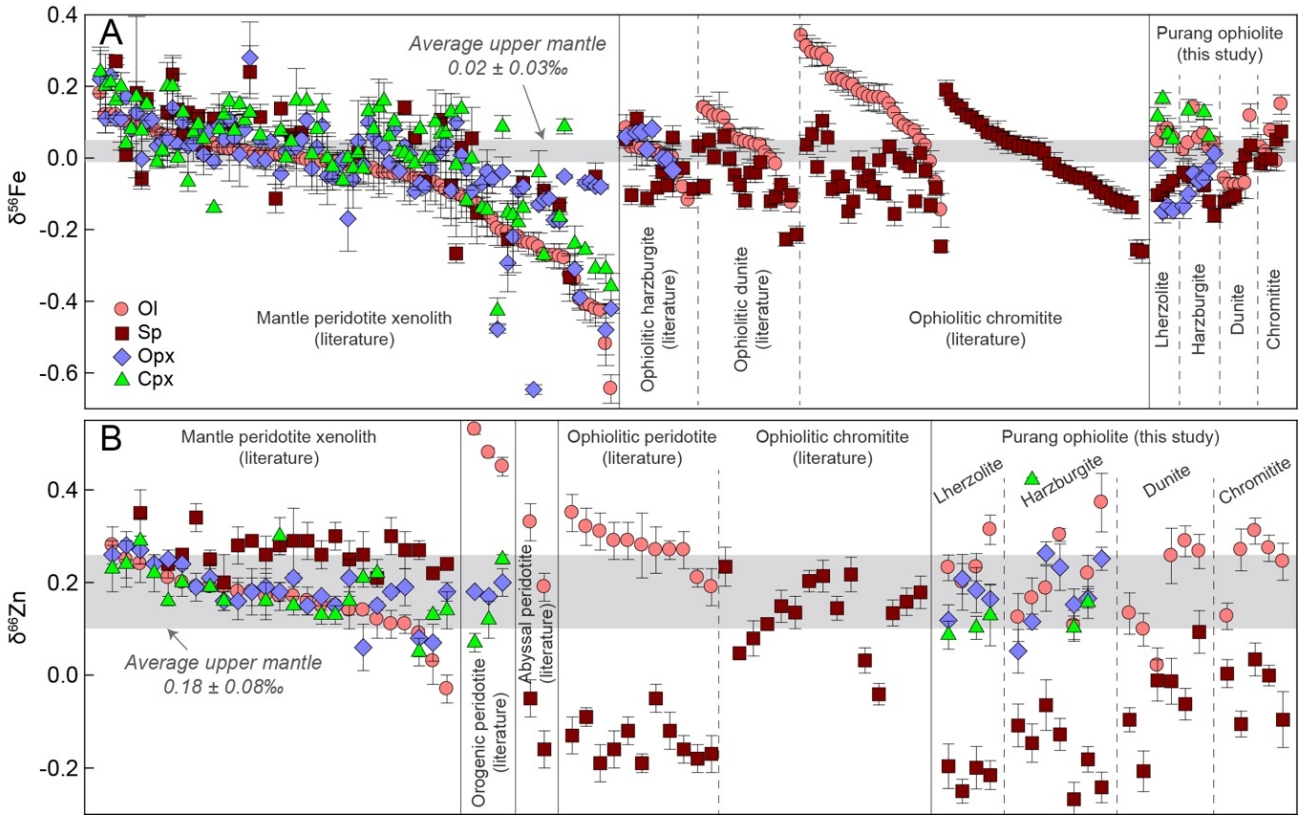

Figure 3. Fe and Zn isotope compositions of mineral pairs in mantle peridotite xenoliths, ophiolites, and orogenic and abyssal peridotites. Purang data are from this study, and others are literature compilations. (A) δ^{56}Fe values, with ophiolitic silicates showing heavier isotopes relative to spinel, contrasting with the equilibrium sequence in xenoliths. (B) δ^{66}Zn values, highlighting lighter spinel and heavier silicates in ophiolites compared to xenoliths, deviating from upper mantle average. Average upper mantle values of Fe and Zn isotopes are from Weyer and Ionov (2007) and Sun et al. (in press), respectively. Data sources for δ^{56}Fe: peridotite xenolith, An et al. (2017), Beard and Johnson (2004), Huang et al. (2011), Macris et al. (2015), Williams et al. (2005), Williams and Bizimis (2014), Zhao et al. (2010, 2012, 2015, 2017); ophiolitic rocks, Chen et al. (2015), Su et al. (2021), Xiao et al. (2016), Xiong et al. (2025), Zhang et al. (2017, 2019). Data sources for δ^{66}Zn: peridotite xenolith, Fang et al. (2022), Z.-Z. Wang et al. (2017); orogenic peridotites, Fang et al. (2022); abyssal peridotites, Yang et al. (2021); ophiolitic rocks, Lian et al. (2024), Yang et al. (2021).

due to Zn's lower abundance relative to Fe, which facilitates greater isotope sensitivity to modification.

Serpentinization also influences isotope signatures in some Purang samples. Serpentinized dunites and chromitites (e.g., PL14-5-19, PL14-5-8; figs. 2F, H, S1) show lighter Fe isotope compositions in olivine compared to coexisting spinel (fig. 4A). This shift likely results from serpentinization-driven oxidation and preferential leaching of heavier Fe isotopes from olivine (Scott et al., 2017; B.-X. Su et al., 2015). Zinc isotopes, unaffected by valence changes, exhibit minimal fractionation during serpentinization (fig. 3B; S.-A. Liu et al., 2019; Yang et al., 2021). Excluding these outliers, Purang minerals display a positive correlation between δ^{56}Fe and δ^{66}Zn (fig. 4B), reflecting similar geochemical behaviors of Fe and Zn isotope systematics.

Mineral chemistry further informs isotope variability. Spinel, rich in total FeO (fig. S2A), Fe^{3+}, and Zn (500–1700 ppm) compared to olivine (intermediate FeO, Zn ~20–95 ppm) and pyroxenes (Zn ~10–30 ppm; B. X. Su et al., 2019), is less abundant but more resistant to isotope modification. Olivine, dominant in modal abundance, lacks Fe^{3+} and shows larger Fe-Zn isotope variations (figs. 3, 4B).

5.3. Influences of partial melting, melt metasomatism, and magma differentiation on inter-sample Fe-Zn isotope variations

5.3.1. Partial melting and melt metasomatism in peridotites

Both continental and oceanic lithospheric mantle undergo partial melting and metasomatism, which influence Fe and Zn isotope compositions. Partial melting typically enriches residual rocks and minerals in lighter isotopes (Z.-Z. Wang et al., 2017; Weyer & Ionov, 2007), while melt metasomatism normally introduces heavier compositions to re-equilibrated phases (Sun et al., in press; Weyer & Ionov, 2007). These processes primarily contribute to inter-sample isotope variability. Spinel Cr# and olivine FeO content serve as proxies for mantle melting and metasomatism. Spinel from mantle peridotite xenoliths and ophiolitic peridotites, including Purang samples, shows a negative correlation between δ^{56}Fe and Cr#, suggesting retention of partial melting and metasomatism signatures (fig. 4C). The scattered distribution of xenolithic spinel likely reflects metasomatic melts with variable Fe isotope compositions (Poitrasson et al., 2013; Zhao et al., 2012, 2015). In contrast, olivine Fe isotope compositions show no clear correlations with FeO content in either xenoliths or ophiolites (fig. S2). Limited Zn isotope data for xenolithic olivine align with partial melting- metasomatism trends, whereas olivine from ophiolitic, abyssal and orogenic peridotites deviates toward lower FeO and higher δ^{66}Zn values (fig. 4D). This indicates that peridotitic olivine in oceanic lithospheric mantle is more susceptible to isotope disturbance, preserving fewer primary melting or metasomatism signatures compared to spinel (Pan et al., 2025; B.-X. Su et al., 2018, 2020, 2023; Zhang et al., 2019, 2024). However, neither processes can reverse the inter-mineral isotope sequence as observed in ophiolitic rocks (fig. 3).

5.3.2. Effect of magma differentiation on mineral isotopes of chromitites and dunites

Chromitites and dunites in ophiolites, being of cumulate origin in magma chambers and conduits (e.g., B.-X. Su et al., 2020, 2023, 2026), exhibit distinct isotope trends. Spinel in these rocks shows increasing δ^{56}Fe and δ^{66}Zn with higher $Fe^{3+}/(Fe^{3+}+Fe^{2+})$ ratios, a marker of magma differentiation (fig. 4E). These spinels are distinguished from those in peridotite xenoliths and oceanic mantle peridotites by intermediate δ^{66}Zn values and FeO contents (fig. S2C). Cumulus olivine Zn isotopes follow magma differentiation trends (fig. 4D), but their δ^{56}Fe values diverge from this path (fig. 4F), suggesting that significant post-crystallization isotope modification in olivine, which is discussed below.

5.4. Influences of subsolidus exchange and hydrous fluid-mediated diffusion on reversed inter-mineral Fe-Zn isotopes

Element diffusion, particularly during subsolidus exchange, is a well-established mechanism for isotope fractionation, with lighter isotopes diffusing faster than heavier ones (e.g., Dauphas et al., 2010; Sio et al., 2013; Teng et al., 2011). This process accounts for the observed Fe, Zn, Cr, and Mg isotope fractionation between spinel and olivine in layered intrusions (Bai et al., 2019, 2021) and ophiolites (Xiao et al., 2016, 2023). During subsolidus exchange, Fe and Cr migrate from olivine to spinel, while Mg moves in the opposite direction, resulting in elevated δ^{56}Fe and δ^{53}Cr values and reduced δ^{26}Mg in olivine, with converse trends in spinel. The extent of fractionation depends on mineral modal abundances, spatial relationships, and element concentrations (Pagé & Barnes, 2009; B.-X. Su et al., 2021, 2026; Xiao et al., 2016, 2023). In peridotites, low abundances of spinel (<5%) and their high FeO and Zn contents make it highly susceptible to isotope modification, while in chromitites, variable abundances of olivine and their lower FeO and Zn contents amplify its sensitivity to exchange (figs. 2E–H, S2). Olivine in oceanic lithospheric mantle peridotites and dunite cumulates deviates significantly from partial melting and metasomatism trends, aligning instead with patterns of element exchange (figs. 4D, F, S2B). Spinel in ophiolitic chromitites shows notably δ^{56}Fe variability at a given $Fe^{3+}/(Fe^{3+}+Fe^{2+})$ ratio, consistent with subsolidus exchange effects (fig. 4E).

High-temperature dry diffusion (e.g., subsolidus Fe-Mg exchange) can produce reversed fractionation (Bai et al., 2019, 2021; Xiao et al., 2016) but is limited by grain boundary distances (<1 mm) and requires long residence times (>10^7 years at 900 °C; Sio et al., 2013), which fails to account for the widespread reversal in ophiolites lacking close mineral contacts (fig. 5A–C). Deformation-enhanced diffusion (e.g., via dislocations) may amplify rates but still relies on proximity and does not explain pervasive patterns across unstrained samples (e.g., Purang lherzolites; fig. 2). Oxygen fugacity changes (e.g., fO_2 increase during serpentinization) affect Fe valence and isotopes but not Zn, which lacks redox sensitivity (S.-A. Liu et al., 2019; Muir et al.,

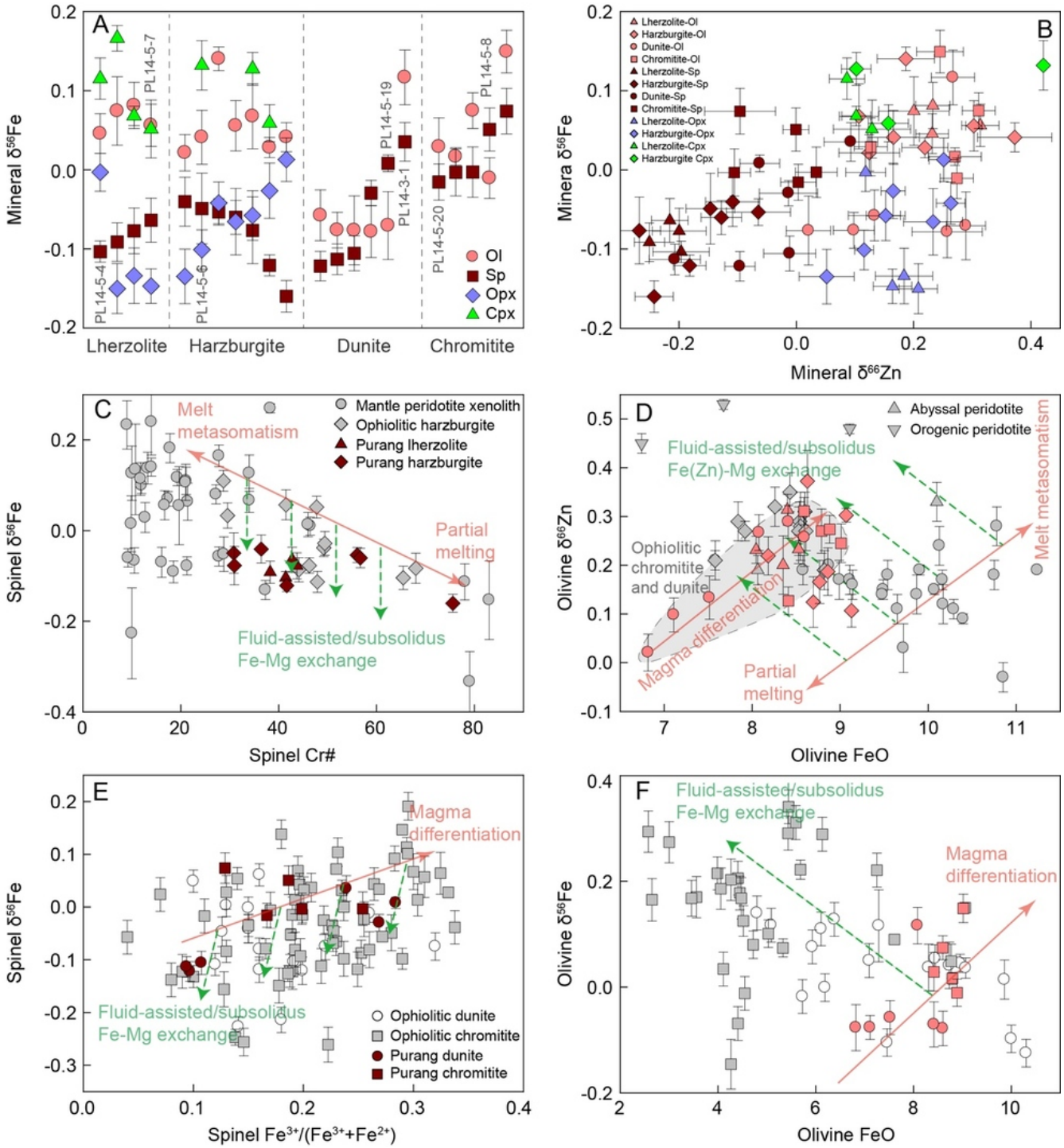

Figure 4. (A) Fe isotope compositions of minerals in samples from the Purang ophiolite, with sample numbers corresponding to those in fig. 2. (B) Plot of FeO vs. δ^{56}Fe for minerals from the Purang ophiolite, illustrating isotopic variations. (C) Cr# vs. δ^{56}Fe for spinel from mantle peridotite xenoliths and ophiolitic lherzolites and harzburgites, reflecting partial melting and metasomatism signatures. (D) FeO vs. δ^{66}Zn for olivine from ophiolitic rocks, abyssal peridotites, orogenic peridotites, and mantle peridotite xenoliths, highlighting deviations in oceanic mantle. (E) $Fe^{3+}/(Fe^{3+}+Fe^{2+})$ vs. δ^{56}Fe for spinel from ophiolitic dunites and chromitites, showing element exchange effects. (F) FeO vs. δ^{56}Fe for olivine from ophiolitic dunites and chromitites, indicating post-crystallization isotope modification. Trends of partial melting, melt metasomatism, fluid-assisted/subsolidus Fe(Zn)-Mg exchange, and magma differentiation are defined based on Fe and Zn isotope geochemical behavior. Purang data are from this study, and others are literature compilations with same data sources in fig. 3.

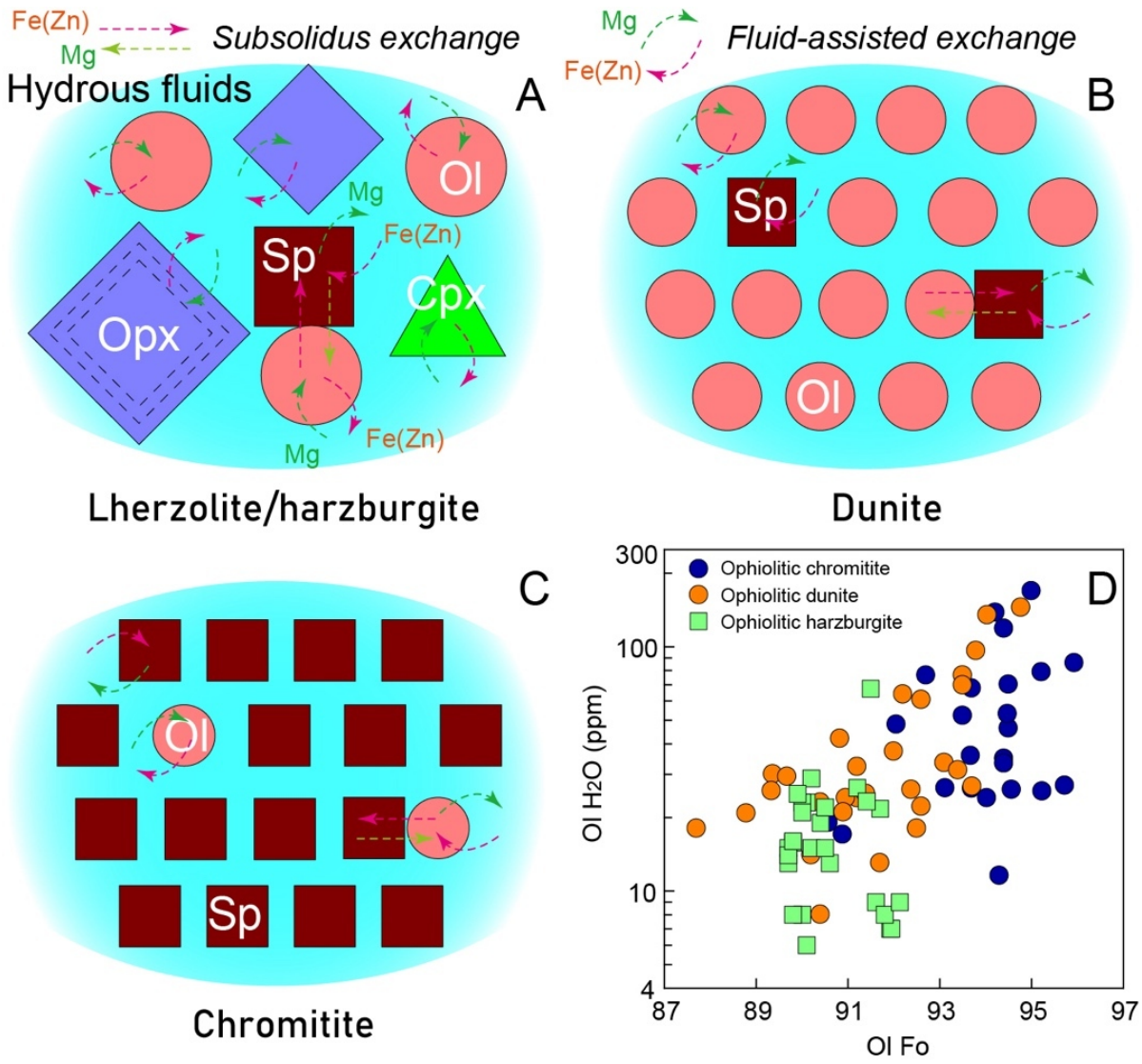

Figure 5. (A–C) Schematic model of fluid-assisted element exchange and subsolidus diffusion in various lithologies of the oceanic lithospheric mantle. Magnesium diffuses from spinel to silicates via a hydrous fluid medium, while Fe and Zn move in the opposite direction, resulting in reversed Fe and Zn isotope fractionation. Large orthopyroxene grains in lherzolites and harzburgites may experience limited isotopic modification. (D) Correlation between H_2O content and Fo in olivine from ophiolitic rocks, highlighting hydration-driven compositional changes (after Cui et al., 2025; B.-X. Su et al., 2025; and references therein).

2023). The coupled reversed Fe-Zn (and Cr) fractionation uniquely points to hydrous fluid mediation, as fluids enable long-range transport and selective element mobility (e.g., Fe^{2+} and Zn substituting Mg in lattices; Lian et al., 2024; Yang et al., 2021).

We note that H_2O can significantly enhance diffusion rates in nominally anhydrous minerals at subsolidus temperatures (800–1000 °C), as demonstrated by experimental studies (e.g., Demouchy & Bolfan-Casanova, 2016; Nishi, 2015). Hydrous fluids facilitate element mobility over distances of centimeters to meters, far exceeding dry subsolidus diffusion limits (e.g., Bai et al., 2021; Sio et al., 2013). Experimental diffusion models indicate that H_2O contents of 10–50 ppm increase Fe-Mg interdiffusion coefficients in olivine by 1–2 orders of magnitude (e.g., Hier-Majumder et al., 2005), sufficient to produce the observed $\Delta^{56}Fe_{silicate\text{-}spinel}$ of 0.1–0.3‰ over timescales of 10^4–10^6 years at 900 °C. Consequently, to account for the pervasive reversed fractionation, hydrous fluid-assisted diffusion is critical (B. X. Su et al., 2021; B.-X. Su et al., 2021). Highly mobile hydrous fluids overcome spatial barriers of subsolidus exchange, facilitating large-scale element transport across minerals (fig. 5A–C). This process drives significant Fe enrichment in spinel and depletion in olivine, particularly pronounced in peridotites and chromitites, respectively (fig. 5A–C; B. X. Su et al., 2021). Zinc, with geochemical behavior similar to Fe, is co-mobilized or substitute for Mg in mineral lattices, leading to lighter Fe-Zn isotope compositions in spinel relative to silicates (fig. 4; Lian et al., 2024; Yang et al., 2021). Petrographic evidence, including spinel zoning and inter-grain compositional heterogeneity, supports hydrous fluid-mediated exchange (Gamal

El Dien et al., 2019; Pan et al., 2022; B.-X. Su et al., 2023, 2026). Elevated H_2O contents in ophiolitic olivine, positively correlated with Fo values, further confirm hydration-driven compositional changes (Cui et al., 2025; B.-X. Su et al., 2025, 2026). Additionally, lower $\delta^{18}O$ values in ophiolitic spinel (1.04–4.87‰) compared to silicates (e.g., olivine: 4.90–6.68‰) in dunites and harzburgites indicate extensive fluid interaction (Pan et al., 2025). The intergrowth of clinopyroxene and spinel in ophiolitic rocks (B. X. Su et al., 2019) results in comprehensive element exchange and thus heavier Fe-Zn isotope compositions in clinopyroxene (fig. 3). These observations suggest that spinel in ophiolitic mantle peridotites rarely retains pristine paleo-oceanic mantle signatures, highlighting its sensitivity to fluid-mediated modification and challenging its use as a reliable petrogenetic indicator. We acknowledge that these estimates are based on representative ophiolitic data, future direct analyses of H_2O contents on our mineral separates would provide even tighter constraints on sample-specific variability.

5.5. Extensive hydration in oceanic lithospheric mantle

Recent studies of ophiolitic peridotites have revealed hydration as a pervasive and transformative process in the oceanic lithospheric mantle, with profound implications for its geochemical and physical properties. Traditionally viewed as a minor, surface-related phenomenon associated with hydrothermal alteration or late-stage serpentinization (Greenberger et al., 2021; Gruau et al., 1998; Sanfilippo et al., 2025), hydration is now recognized as a deep-seated process (Cui et al., 2025; Demouchy et al., 2015; Nishi, 2015; Schmädicke et al., 2018; B.-X. Su et al., 2023, 2025). Isotopic evidence, including reversed Fe and Zn isotope fractionation between spinel and silicates, contrasting with equilibrium patterns in continental mantle xenoliths, indicates fluid-mediated element exchange as a common feature of oceanic mantle rocks (ophiolites, abyssal, and orogenic peridotites) (fig. 3; Chen et al., 2019; Fang et al., 2022; Yang et al., 2021). Petrographic features, such as zoning in spinel, compositional heterogeneity, and variable oxygen isotope ratios (e.g., spinel $\delta^{18}O$: 1.04–4.87‰ vs. olivine: 4.90–6.68‰), alongside the presence of hydrous minerals like amphibole, confirm widespread hydrous fluid infiltration (Gamal El Dien et al., 2019; C.-Z. Liu et al., 2010; Pan et al., 2022, 2025; B.-X. Su et al., 2020, 2023, 2026).

Hydrous fluids in the oceanic mantle originate from multiple sources. In supra-subduction zone (SSZ)-type ophiolites like Purang, slab-derived fluids dominate during forearc extension (post-melting, pre-obduction) (C.-Z. Liu et al., 2010; Pan et al., 2025; B.-X. Su et al., 2023). In contrast, mid-ocean ridge (MOR)-type abyssal peridotites may involve asthenospheric fluids at the lithosphere base (Hirschmann & Kohlstedt, 2012). Post-obduction serpentinization cannot explain the coupled Fe-Zn reversal, as it primarily affects Fe isotopes via oxidation without reversing Zn isotope fractionation (S.-A. Liu et al., 2019). Chromitite formation releases hydrous fluids, as observed in ophiolites (Cui et al., 2025; Matveev & Ballhaus, 2002; B. X. Su et al., 2021; B.-X. Su et al., 2020, 2021, 2025, 2026) and layered intrusions like the Stillwater Complex, which exhibits reversed Fe-Cr isotope fractionation (Bai et al., 2019, 2021, 2024). In ophiolites lacking significant chromite deposits, such as Purang, subduction-related fluids from slab dehydration infiltrate the mantle wedge, driving hydration and isotopic resetting (Gose & Schmädicke, 2021; B.-X. Su et al., 2023). Additionally, asthenospheric upwelling introduces minor hydrous fluids due to water gradient (Hirschmann & Kohlstedt, 2012), further hydrating the lithosphere base (Cui et al., 2025; B.-X. Su et al., 2025). These diverse sources underscore the complex, multi-stage nature of mantle hydration.

6. CONCLUSION

While pronounced in SSZ ophiolites like Purang, the reversal of inter-mineral Fe-Zn isotope fractionation is evident in MOR-type abyssal peridotites (albeit with fewer data; Yang et al., 2021), indicating a potentially fundamental oceanic lithospheric mantle trait. Future studies on pristine abyssal samples will test its ubiquity. Driven by diverse fluid sources, including chromitite formation, subduction-related dehydration, and asthenospheric upwelling, this hydration facilitates extensive fluid-mediated element exchange, profoundly altering mantle geochemistry. Historically underestimated due to methodological limitations and an overemphasis on anhydrous processes, hydration is now recognized as a deep-seated, integral component of mantle evolution, impacting supra-subduction and likely abyssal settings. Its effects extend beyond geochemical overprinting to influence mantle rheology, volatile cycling, and geophysical properties. Recognizing the scale and significance of hydration is critical for refining models of oceanic lithospheric mantle formation, subduction zone dynamics, and global tectonic and geochemical evolution. Hydration emerges not as a secondary process but as a primary architect of the oceanic mantle's physiochemical framework.

Acknowledgments

We appreciate two anonymous reviewers for their constructive comments, which significantly improve the quality of the paper. This study was supported by special fund of Deep Earth Probe and Mineral Resources Exploration-National Science and Technology Major Project of China (2025ZD1006104), National Natural Science Foundation of China (92462305, 42350001), and China Geological Survey ((2025)02-032-01-06).

Author contributions

B.-X.S. and Y.X. designed and led the project. J.W., S.-Q.Z. and Q.-Q.P. conducted the analyses. B.-X.S. wrote the manuscript with inputs from Y.X., J.W., Q.-Q.P., and S.-Q.Z. All authors contributed the interpretation of the results.

Data availability

Data are available through https://figshare.com/ at http://10.6084/m9.figshare.29436158.

Supplemantary information

https://doi.org/10.17632/y6sz2n5tys.1

Editor: C. Page Chamberlain, Associate Editor: Guochun Zhao

Submitted: November 08, 2025 EDT. Accepted: April 07, 2026 EDT. Published: April 22, 2026 EDT.

REFERENCES

An, Y., Huang, J.-X., Griffin, W. L., Liu, C., & Huang, F. (2017). Isotopic composition of Mg and Fe in garnet peridotites from the Kaapvaal and Siberian cratons. *Geochimica et Cosmochimica Acta*, *200*, 167–185. https://doi.org/10.1016/j.gca.2016.11.041

Bai, Y., Cui, M.-M., Su, B.-X., Liu, X., Xiao, Y., Robinson, P. T., & Gu, X.-Y. (2024). FTIR study of H2O in silicate minerals and mineral inclusions in chromite from the Peridotite Zone of the Stillwater Complex: evidence for chromitite formation in a H2O-rich environment. *Geological Society of America Bulletin*, *136*(3–4), 1661–1674. https://doi.org/10.1130/B36733.1

Bai, Y., Su, B.-X., Xiao, Y., Chen, C., Cui, M.-M., He, X.-Q., Qin, L.-P., & Charlier, B. (2019). Diffusion-driven chromium isotope fractionation in minerals of ultramafic cumulate minerals: elemental and isotopic evidence from the Stillwater Complex. *Geochimica et Cosmochimica Acta*, *263*, 167–181. https://doi.org/10.1016/j.gca.2019.07.052

Bai, Y., Su, B.-X., Xiao, Y., Cui, M.-M., & Charlier, B. (2021). Magnesium and iron isotopic evidence of inter-mineral diffusion in ultramafic cumulates of the Peridotite Zone, Stillwater Complex. *Geochimica et Cosmochimica Acta*, *292*, 152–169. https://doi.org/10.1016/j.gca.2020.09.023

Beard, B. L., & Johnson, C. M. (2004). Inter-mineral Fe isotope variations in mantle-derived rocks and implications for the Fe geochemical cycle. *Geochimica et Cosmochimica Acta*, *68*(22), 4727–4743. https://doi.org/10.1016/j.gca.2004.04.023

Chen, C., Su, B.-X., Uysal, I., Avcı, E., Zhang, P.-F., Xiao, Y., & He, Y.-S. (2015). Iron isotopic constraints on the origin of peridotite and chromitite in the Kızıldağ ophiolite, southern Turkey. *Chemical Geology*, *417*, 115–124. https://doi.org/10.1016/j.chemgeo.2015.10.001

Chen, C., Su, B.-X., Xiao, Y., Sakyi, P. A., He, X.-Q., Pang, K.-N., Uysal, I., Avcı, E., & Qin, L.-P. (2019). High-temperature chromium isotope fractionation and its implications: Constraints from Kizildag ophiolite, SE Turkey. *Lithos*, *342–343*, 361–369. https://doi.org/10.1016/j.lithos.2019.05.038

Cui, M.-M., Su, B.-X., Bai, Y., Zhang, W.-F., & Pan, Q.-Q. (2025). Hydration disparities in crustal and mantle magmatic systems: Insights from the Stillwater complex, Alaskan-type complexes, and Pozantı-Karsantı ophiolite. *Lithos*, *518–519*, 108318. https://doi.org/10.1016/j.lithos.2025.108318

Dauphas, N., Teng, F.-Z., & Arndt, N. T. (2010). Magnesium and iron isotopes in 2.7 Ga Alexo komatiites: mantle signatures, no evidence for Soret diffusion, and identification of diffusive transport in zoned olivine. *Geochimica et Cosmochimica Acta*, *74*(11), 3274–3291. https://doi.org/10.1016/j.gca.2010.02.031

Demouchy, S., & Bolfan-Casanova, N. (2016). Distribution and transport of hydrogen in the lithospheric mantle: a review. *Lithos*, *240–243*, 402–425. https://doi.org/10.1016/j.lithos.2015.11.012

Demouchy, S., Ishikawa, A., Tommasi, A., Alard, O., & Keshav, S. (2015). Characterization of hydration in the mantle lithosphere: Peridotite xenoliths from the Ontong Java Plateau as an example. *Lithos*, *212–215*, 189–201. https://doi.org/10.1016/j.lithos.2014.11.005

Fang, S.-B., Huang, J., Zhang, X.-C., Ionov, D. A., Zhao, Z.-F., & Huang, F. (2022). Zinc isotope fractionation in mantle rocks and minerals, and a revised δ^{66}Zn value for the Bulk Silicate Earth. *Geochimica et Cosmochimica Acta*, *338*, 79–92. https://doi.org/10.1016/j.gca.2022.10.017

Gamal El Dien, H., Arai, S., Doucet, L.-S., Li, Z.-X., Kil, Y., Fougerouse, D., Reddy, S. M., Saxey, D. W., & Hamdy, M. (2019). Cr-spinel records metasomatism not petrogenesis of mantle rocks. *Nature Communications*, *10*(1), 5103. https://doi.org/10.1038/s41467-019-13117-1

Gose, J., & Schmädicke, E. (2021). Water in the supra-subduction-zone mantle of the Mariana-Izu-Bonin forearc: Constraints from peridotitic orthopyroxene. *Geochemistry, Geophysics, Geosystems*, *22*(4), e2020GC009586. https://doi.org/10.1029/2020GC009586

Greenberger, R. N., Harris, M., Ehlmann, B. L., Crotteau, M. A., Kelemen, P. B., Manning, C. E., Teagle, D. A. H., & the Oman Drilling Project Science Team. (2021). Hydrothermal alteration of the ocean crust and patterns in mineralization with depth as measured by micro-imaging infrared spectroscopy. *Journal of Geophysical Research: Solid Earth*, *126*(8), e2021JB021976. https://doi.org/10.1029/2021JB021976

Gruau, G., Bernard-Griffiths, J., & Lécuyer, C. (1998). The origin of U-shaped rare earth patterns in ophiolite peridotites: assessing the role of secondary alteration and melt/rock reaction. *Geochimica et Cosmochimica Acta*, *62*(21–22), 3545–3560. https://doi.org/10.1016/S0016-7037(98)00250-6

Hebei Institute of Geological Survey. (2006). *1:250,000 geological map of Purang County* [Map]. Hebei Institute of Geological Survey.

Hier-Majumder, S., Anderson, I. M., & Kohlstedt, D. L. (2005). Influence of protons on Fe-Mg interdiffusion in olivine. *Journal of Geophysical Research: Solid Earth*, *110*(B2), B02202. https://doi.org/10.1029/2004JB003292

Hirschmann, M., & Kohlstedt, D. (2012). Water in Earth's mantle. *Physics Today*, *65*, 40–45. https://doi.org/10.1063/PT.3.1476

Huang, F., Zhang, Z., Lundstrom, C. C., & Zhi, X. C. (2011). Iron and magnesium isotope compositions of peridotite xenoliths from Eastern China. *Geochimica et Cosmochimica Acta*, *75*(12), 3318–3334. https://doi.org/10.1016/j.gca.2011.03.036

Lian, D., Liu, F., Cai, P., Wu, W., Li, J., Majka, J., Xu, Z., & Yang, J. (2024). Osmium and zinc isotope constraints on the origin of chromitites from the Yarlung-Zangbo ophiolites, Tibet, China. *Mineralium Deposita*, *59*(6), 1089–1107. https://doi.org/10.1007/s00126-024-01252-9

Liu, C.-Z., Wu, F.-Y., Wilde, S. A., Yu, L.-J., & Li, J.-L. (2010). Anorthitic plagioclase and pargasitic amphibole in mantle peridotites from the Yungbwa ophiolite (southwestern Tibetan Plateau) formed by hydrous melt metasomatism. *Lithos*, *114*(3–4), 413–422. https://doi.org/10.1016/j.lithos.2009.10.008

Liu, F., Yang, J. -s., Dilek, Y., Xu, Z.-Q., Xu, X.-Z., Liang, F.-H., Chen, S.-Y., & Lian, D.-Y. (2015). Geochronology and geochemistry of basaltic lavas in the Dongbo and Purang ophiolites of the Yarlung-Zangbo Suture zone: Plume-influenced continental margin-type oceanic lithosphere in southern Tibet. *Gondwana Research*, *27*(2), 701–718. https://doi.org/10.1016/j.gr.2014.08.002

Liu, J., Xia, Q.-K., Kuritani, T., Hanski, E., & Yu, H.-R. (2017). Mantle hydration and the role of water in the generation of large igneous provinces. *Nature Communications*, *8*(1), 1824. https://doi.org/10.1038/s41467-017-01940-3

Liu, S.-A., Liu, P.-P., Lv, Y., Wang, Z.-Z., & Dai, J.-G. (2019). Cu and Zn isotope fractionation during oceanic alteration: Implications for Oceanic Cu and Zn cycles. *Geochimica et Cosmochimica Acta*, *257*, 191–205. https://doi.org/10.1016/j.gca.2019.04.026

Macris, C. A., Manning, C. E., & Young, E. D. (2015). Crystal chemical constraints on inter-mineral Fe isotope fractionation and implications for Fe isotope disequilibrium in San Carlos mantle xenoliths. *Geochimica et Cosmochimica Acta*, *154*, 168–185. https://doi.org/10.1016/j.gca.2015.01.024

Matveev, S., & Ballhaus, C. (2002). Role of water in the origin of podiform chromitite deposits. *Earth and Planetary Science Letters*, *203*(1), 235–243. https://doi.org/10.1016/S0012-821X(02)00860-9

Muir, J. M. R., Jollands, M., & Zhang, F. W. (2023). The oxidation states of iron in dry and wet olivine: A thermodynamic model. *Journal of Geophysical Research: Solid Earth*, *128*(9), e2023JB026840. https://doi.org/10.1029/2023JB026840

Nishi, M. (2015). Mantle hydration. *Nature Geoscience*, *8*(1), 9–10. https://doi.org/10.1038/ngeo2326

Pagé, P., & Barnes, S. J. (2009). Using trace elements in chromites to constrain the origin of podiform chromitites in the Thetford Mines ophiolite, Quebec, Canada. *Economic Geology*, *104*(7), 997–1018. https://doi.org/10.2113/econgeo.104.7.997

Pan, Q.-Q., Xiao, Y., Su, B.-X., Fu, B., Zhang, P.-F., Robinson, P. T., Uysal, I., & Williams, I. S. (2025). Oxygen isotopes of Cr-spinel as a pathfinder for metasomatism in mantle peridotites. *Journal of Petrology*, *66*(6), egaf055. https://doi.org/10.1093/petrology/egaf055

Pan, Q.-Q., Xiao, Y., Su, B.-X., Liu, X., Robinson, P. T., Uysal, I., Zhang, P.-F., & Sakyi, P. A. (2022). Amphibole as a witness of chromitite formation and fluid metasomatism in ophiolites. *American Mineralogist*, *107*(2), 294–305. https://doi.org/10.2138/am-2021-7593

Poitrasson, F., Delpech, G., & Grégoire, M. (2013). On the iron isotope heterogeneity of lithospheric mantle xenoliths: implications for mantle metasomatism, the origin of basalts and the iron isotope composition of the Earth. *Contributions to Mineralogy and Petrology*, *165*(6), 1243–1258. https://doi.org/10.1007/s00410-013-0856-7

Roskosz, M., Sio, C. K. I., Dauphas, N., Bi, W., Tissot, F. L. H., Hu, M. Y., Zhao, J., & Alp, E. E. (2015). Spinel-olivine-pyroxene equilibrium iron isotopic fractionation and applications to natural peridotites. *Geochimica et Cosmochimica Acta*, *169*, 184–199. https://doi.org/10.1016/j.gca.2015.07.035

Sanfilippo, A., Pandey, A., Akizawa, N., Poulaki, E., Cunningham, E., Bickert, M., Lei, C., Vannucchi, P., Estes, E. R., Malinverno, A., Abe, N., Di Stefano, A., Filina, I. Y., Fu, Q., Gontharet, S. B. L., Kearns, L. E., Koorapati, R. K., Loreto, M. F., Magri, L., … Zitellini, N. (2025). Heterogeneous Earth's mantle drilled at an embryonic ocean. *Nature Communications*, *16*(1), 2016. https://doi.org/10.1038/s41467-025-57121-0

Schauble, E. A., Rossman, G. R., & Taylor, H. P., Jr. (2001). Theoretical estimates of equilibrium Fe-isotope fractionation from vibrational spectroscopy. *Geochimica et Cosmochimica Acta*, *65*(15), 2487–2497. https://doi.org/10.1016/s0016-7037(01)00600-7

Schmädicke, E., Gose, J., & Stalder, R. (2018). Water in abyssal peridotite: Why are melt-depleted rocks so water rich? *Geochemistry, Geophysics, Geosystems*, *19*(6), 1824–1843. https://doi.org/10.1029/2017GC007390

Scott, S. R., Sims, K. W. W., Frost, B. R., Kelemen, P. B., Evans, K. A., & Swapp, S. M. (2017). On the hydration of olivine in ultramafic rocks: Implications from Fe isotopes in serpentinites. *Geochimica et Cosmochimica Acta*, *215*, 105–121. https://doi.org/10.1016/j.gca.2017.07.011

Shen, J., Qin, L., Fang, Z., Zhang, Y., Liu, J., Liu, W., Wang, F., Xiao, Y., Yu, H., & Wei, S. (2018). High-temperature inter-mineral Cr isotope fractionation: A comparison of ionic model predictions and experimental investigations of mantle xenoliths from the North China Craton. *Earth and Planetary Science Letters*, *499*, 278–290. https://doi.org/10.1016/j.epsl.2018.07.041

Sio, C. K. I., Dauphas, N., Teng, F.-Z., Chaussidon, M., Helz, R. T., & Roskosz, M. (2013). Discerning crystal growth from diffusion profiles in zoned olivine by in situ Mg-Fe isotopic analyses. *Geochimica et Cosmochimica Acta*, *123*, 302–321. https://doi.org/10.1016/j.gca.2013.06.008

Su, B. X., Liu, X., Chen, C., Robinson, P. T., Xiao, Y., Zhou, M. F., Bai, Y., Uysal, I., & Zhang, P. F. (2021). A new model for chromitite formation in ophiolites: Fluid immiscibility. *Science China Earth Sciences*, *64*(2), 220–230. https://doi.org/10.1007/s11430-020-9690-4

Su, B. X., Zhou, M. F., Jing, J. J., Robinson, P. T., Chen, C., Xiao, Y., Liu, X., Shi, R. D., Lenaz, D., & Hu, Y. (2019). Distinctive melt activity and chromite mineralization in Luobusa and Purang ophiolites, southern Tibet: Constraints from trace element compositions of chromite and olivine. *Science Bulletin*, *64*(2), 108–121. https://doi.org/10.1016/j.scib.2018.12.018

Su, B.-X., Chen, C., Pang, K.-N., Sakyi, P. A., Uysal, I., Avcı, E., Liu, X., & Zhang, P.-F. (2018). Melt penetration in oceanic lithosphere: Li isotope records from the Pozantı-Karsantı ophiolite in southern Turkey. *Journal of Petrology*, *59*(1), 191–205. https://doi.org/10.1093/petrology/egy023

Su, B.-X., Chen, C., Xiao, Y., Robinson, P. T., Liu, X., Wang, J., Uysal, I., Bai, Y., & Sun, Y. (2021). The critical role of fluid-mediated diffusion in anomalous Fe-Mg-O isotope fractionations in ultramafic rocks of ophiolites. *Journal of Geophysical Research: Solid Earth*, *126*(4), e2020JB020632. https://doi.org/10.1029/2020JB020632

Su, B.-X., Liu, X., Xiao, Y., Uysal, I., & Pan, Q.-Q. (2026). Characterization of stratiform-like chromite deposits in ophiolites and their genetic link with podiform chromitites. *Journal of the Geological Society*, *183*(3), jgs2025-180. https://doi.org/10.1144/jgs2025-180

Su, B.-X., Pan, Q.-Q., Xiao, Y., Jing, J.-J., Robinson, P. T., Uysal, I., Liu, X., & Liu, J.-G. (2023). Mantle peridotites of ophiolites rarely preserve reliable records of paleo-oceanic lithospheric mantle. *Earth-Science Reviews*, *244*, 104544. https://doi.org/10.1016/j.earscirev.2023.104544

Su, B.-X., Robinson, P. T., Chen, C., Xiao, Y., Melcher, F., Bai, Y., Gu, X. Y., Uysal, I., & Lenaz, D. (2020). The occurrence, origin and fate of water in podiform chromitites. *American Mineralogist*, *105*(6), 894–903. https://doi.org/10.2138/am-2020-7270

Su, B.-X., Teng, F.-Z., Hu, Y., Shi, R.-D., Zhou, M.-F., Zhu, B., Liu, F., Gong, X.-H., Huang, Q.-S., Xiao, Y., Chen, C., & He, Y.-S. (2015). Iron and magnesium isotope fractionation in oceanic lithosphere and sub-arc mantle: perspectives from ophiolites. *Earth and Planetary Science Letters*, *430*, 523–532. https://doi.org/10.1016/j.epsl.2015.08.020

Su, B.-X., Uysal, I., Akmaz, R. M., Pan, Q.-Q., Demir, Y., Ackerman, L., & Robinson, P. T. (in press). Chromite as a key player on highly siderophile elements and osmium isotope compositions of the refractory mantle. *Geochimica et Cosmochimica Acta*. https://doi.org/10.1016/j.gca.2025.04.026

Su, B.-X., Zhang, W.-F., Pan, Q.-Q., Bai, Y., Cui, M.-M., Liu, X., Uysal, I., Xia, X.-P., & Gu, X.-Y. (2025). Water storage in the refractory lithospheric mantle. *Geochemical Perspectives Letters*, *36*, 23–27. https://doi.org/10.7185/geochemlet.2530

Sun, P., Niu, Y., Chen, Y., Duan, M., Li, D., Chen, S., Guo, P., Gong, H., & Wang, X. (in press). Large zinc isotope variations in eastern Pacific seamount basalts as a result of mantle metasomatism. *Geochimica et Cosmochimica Acta*. https://doi.org/10.1016/j.gca.2025.07.031

Teng, F.-Z., Dauphas, N., Helz, R. T., Gao, S., & Huang, S. (2011). Diffusion-driven magnesium and iron isotope fractionation in Hawaiian olivine. *Earth and Planetary Science Letters*, *308*(3–4), 317–324. https://doi.org/10.1016/j.epsl.2011.06.003

Wang, J., Tang, D.-M., Su, B.-X., Yuan, Q.-H., Li, W.-J., Gao, B.-Y., Chen, K.-Y., Bao, Z.-A., & Zhao, Y. (2022). High-precision iron isotopic measurements in low resolution using collision cell (CC)-MC-ICP-MS. *Journal of Analytical Atomic Spectrometry*, *37*(9), 1869–1875. https://doi.org/10.1039/D2JA00084A

Wang, J., Tang, D.-M., Yuan, Q.-H., Su, B.-X., Li, W.-J., Gao, B.-Y., Bao, Z.-A., & Zhao, Y. (2023). Zinc isotope measurement by MC-ICP-MS in geological certified reference materials. *Geostandards and Geoanalytical Research*, *47*(4), 969–982. https://doi.org/10.1111/ggr.12499

Wang, Z.-Z., Liu, S.-A., Liu, J., Huang, J., Xiao, Y., Chu, Z.-Y., Zhao, X.-M., & Tang, L. (2017). Zinc isotope fractionation during mantle melting and constraints on the Zn isotope composition of Earth's upper mantle. *Geochimica et Cosmochimica Acta*, *198*, 151–167. https://doi.org/10.1016/j.gca.2016.11.014

Weyer, S., & Ionov, D. A. (2007). Partial melting and melt percolation in the mantle: The message from Fe isotopes. *Earth and Planetary Science Letters*, *259*(1–2), 119–133. https://doi.org/10.1016/j.epsl.2007.04.033

Williams, H. M., & Bizimis, M. (2014). Iron isotope tracing of mantle heterogeneity within the source regions of oceanic basalts. *Earth and Planetary Science Letters*, *404*, 396–407. https://doi.org/10.1016/j.epsl.2014.07.033

Williams, H. M., Peslier, A. H., McCammon, C., Halliday, A. N., Levasseur, S., Teutsch, N., & Burg, J. P. (2005). Systematic iron isotope variations in mantle rocks and minerals: The effects of partial melting and oxygen fugacity. *Earth and Planetary Science Letters*, *235*(1–2), 435–452. https://doi.org/10.1016/j.epsl.2005.04.020

Xiao, Y., Teng, F.-Z., Su, B.-X., Hu, Y., Zhou, M.-F., Zhu, B., Shi, R.-D., Huang, Q.-S., Gong, X.-H., & He, Y.-S. (2016). Iron and magnesium isotopic constraints on the origin of chemical heterogeneity in podiform chromitite from the Luobusa ophiolite, Tibet. *Geochemistry, Geophysics, Geosystems*, *17*(3), 940–953. https://doi.org/10.1002/2015GC006223

Xiao, Y., Yuan, M., Su, B.-X., Chen, C., Bai, Y., Ke, S., Sun, Y., & Robinson, P. T. (2023). The chromite crisis in the evolution of continental magmas and the initial high δ26Mg reservoir. *Journal of Petrology*, *64*(4), egad019. https://doi.org/10.1093/petrology/egad019

Xiong, F., Zoheir, B., Xu, X., Qiu, T., Gui, W., Xie, H., & Yang, J. (2025). Role of mantle dynamics and geochemical diversity in chromitite formation: insights from the Luobusa ophiolite, SW Tibet. *Mineralium Deposita*, *60*(8), 1689–1712. https://doi.org/10.1007/s00126-025-01368-6

Yang, C., Liu, S.-A., Zhang, L., Wang, Z.-Z., Liu, P.-P., & Li, S.-G. (2021). Zinc isotope fractionation between Cr-spinel and olivine and its implications for chromite crystallization during magma differentiation. *Geochimica et Cosmochimica Acta*, *313*, 277–294. https://doi.org/10.1016/j.gca.2021.08.005

Zhang, P.-F., Zhou, M.-F., Liu, Q.-Y., Malpas, J., Robinson, P. T., & He, Y.-S. (2019). Modification of mantle rocks by plastic flow below spreading centers: Fe isotopic and fabric evidence from the Luobusa ophiolite, Tibet. *Geochimica et Cosmochimica Acta*, *253*, 84–110. https://doi.org/10.1016/j.gca.2019.03.008

Zhang, P.-F., Zhou, M.-F., Robinson, P. T., Malpas, J., Yumul, G. P., Jr., Wang, C. Y., & Li, J. (2024). Diversities of chromite mineralization induced by chemo–thermal evolution of the mantle during subduction initiation. *Nature Communications*, *15*, 9385. https://doi.org/10.1038/s41467-024-53508-7

Zhang, P.-F., Zhou, M.-F., Su, B.-X., Uysal, I., Robinson, P. T., Avcı, E., & He, Y.-S. (2017). Iron isotopic fractionation and origin of chromitites in the paleo-Moho transition zone of the Kop ophiolite, NE Turkey. *Lithos*, *268–271*, 65–75. https://doi.org/10.1016/j.lithos.2016.10.019

Zhao, X. M., Zhang, H. F., Zhu, X. K., Tang, S. H., & Tang, Y. J. (2010). Iron isotope variations in spinel peridotite xenoliths from North China Craton: Implications for mantle metasomatism. *Contributions to Mineralogy and Petrology*, *160*, 1–14. https://doi.org/10.1007/s00410-009-0461-y

Zhao, X. M., Zhang, H. F., Zhu, X. K., Tang, S. H., & Yan, B. (2012). Iron isotope evidence for multistage melt-peridotite interactions in the lithospheric mantle of eastern China. *Chemical Geology*, *292–293*, 127–139. https://doi.org/10.1016/j.chemgeo.2011.11.016

Zhao, X. M., Zhang, H. F., Zhu, X. K., Zhu, B., & Chao, H. H. (2015). Effects of melt percolation on iron isotopic variation in peridotites from Yangyuan, North China Craton. *Chemical Geology*, *401*, 96–110. https://doi.org/10.1016/j.chemgeo.2015.02.031

Zhao, X. M., Zhang, Z. F., Huang, S. C., Liu, Y. F., Li, X., & Zhang, H. F. (2017). Coupled extremely light Ca and Fe isotopes in peridotites. *Geochimica et Cosmochimica Acta*, *208*, 368–380. https://doi.org/10.1016/j.gca.2017.03.024

SUPPLEMENTARY MATERIALS

Supplementary materials

Download: https://ajsonline.org/article/160209-reversed-inter-mineral-fe-zn-isotope-fractionation-in-ophiolitic-peridotites-evidence-for-widespread-hydration-of-oceanic-lithospheric-mantle/attachment/339302.docx